

Data-Augmented Contact Model for Rigid Body Simulation

Yifeng Jiang¹ and C. Karen Liu²

Abstract— Accurately modeling contact behaviors for real-world, near-rigid materials remains a grand challenge for existing rigid-body physics simulators. This paper introduces a *data-augmented* contact model that incorporates analytical solutions with observed data to predict the contact impulse between a particular pair of objects (e.g. a specific robot foot contacting a specific surface). The method enhances the expressiveness of the standard Coulomb contact model by learning the contact behaviors from the observed data, while preserving the fundamental contact constraints whenever possible. For example, a classifier is trained to approximate the transitions between static and dynamic frictions, while non-penetration constraint during collision is enforced analytically. Our method computes the aggregated effect of contact at the rigid-body level, removing the exponential dependency on the number of contact points in many exiting contact handling algorithms.

I. INTRODUCTION

While researchers in computer animation and deep reinforcement learning have developed control policies for complex motor skills in simulated environments, this success has not yet led to much real impact in the world of robotics. Theoretically the ability to simulate an infinite number of scenarios, actions, and physical designs should provide a compelling environment for developing effective real-world control policies for motion. Practically, the reality gap, as termed in the robotics community, between virtual simulations and the physical world renders control policies developed primarily from simulations ineffective in real life scenarios.

The accuracy of contact modeling is one of the most important factors that give rise to the reality gap, especially to humanoid locomotion or manipulation in complex, contact-rich environments. Most existing simulators use an idealized Coulomb friction model, an empirical construct to approximate the changes between two physical regimes (static friction vs dynamic friction). The Coulomb friction model assumes linear relationship between normal force and frictional force, ignoring the impact of contact area. Consequently, the material parameters which result in complex physical interaction are lumped to a single friction coefficient that determines the shape of the friction cone. In addition, the computation of contact force also involves approximation and arbitrary decisions. Many existing simulators discretize the friction cone to friction pyramid in order to formulate

a Linear Complementarity Program (LCP). In multiple frictional contact cases, the solutions of LCP are not unique. Depending on the initial guesses and numerical methods used for solving the LCP problem (e.g. Lemke method [1] vs Gauss-Seidel algorithm [2]), the resulting contact forces can be drastically different. These existing issues suggest that an computational contact model grounded by real-world observations can be a desired alternative.

Learning the laws of physics from real-world data is an emerging research area in computer vision, robotics, and computer animation. While recent work has shown that physical phenomena can be approximated by neural networks with vision perception as input, precisely enforcing constraints, such as contacts, remains difficult for these function approximators learned in an end-to-end fashion—the level of precision needed for contact force computation would be extremely difficult to achieve by a learned regression model. Consider a box resting on a table. If the contact force is slightly larger or smaller than the gravitational force, we will start to see the box rattling or sinking into the table without any external force. Such *categorically* incorrect prediction of physics outcomes will be likely to have negative impacts on the development of control policies.

This paper introduces a *data-augmented* contact model that incorporates analytical solutions with empirical data collected for a particular scenario (e.g. a specific robot foot contacting a specific surface), such that the simulated results better match the observed phenomenon. Our approach is built on three key insights. First, we should utilize analytical solutions from first principles whenever possible and only resort to data-driven approach when the phenomenon is less well understood. For example, the contact force that prevents the objects from interpenetrating with each other should be *enforced* by equations instead of *learned* from the data. In contrast, the static friction condition is less well understood and should be modeled and validated by real-world observations. Second, to combine the strengths of data-driven and analytical models, the contact problem can be broken down to two steps: predicting the next contact state (i.e. static, dynamic, or detach) and determining contact forces based on the contact state prediction and current state of the system. We solve the first step by learning a classifier from the observed data and the second step by a combination of learning a regressor and solving constrained systems. Third, we propose to compute the aggregated effect of contact at the rigid-body level, instead of reasoning about each individual contact point. This decision removes the concern of the exponential dependency on the number of contact points in many contact handling routines, which can become

¹Yifeng Jiang is with School of Electrical and Computer Engineering, Georgia Institute of Technology, Atlanta, GA 30332, USA
yjiang340@gatech.edu

²C. Karen Liu is with School of Interactive Computing, Georgia Institute of Technology, Atlanta, GA 30332, USA
karenliu@cc.gatech.edu

intractable when handling complex objects represented by high-resolution meshes.

Our method is not aiming to replace the generic contact handling routine used in general rigid body simulators. Instead, we envision that our method will be used in the real world where learning the contact behaviors of a specific robot part (e.g. the foot or the hand) and a specific surface or object is crucial for the controller design. Our algorithm also allows the rigid body to be used as the contacting part in an articulated system, without retraining the contact model for that rigid body. This implies that the training data for the contact model can be collected using an isolated rigid body, without putting the entire robotic system at risk.

Since the Coulomb friction model is constructed based on empirical evidence, our data-driven approach can be viewed as an alternative empirical model for predicting the contact states and forces for a specific scenario. We evaluate our method on a set of 2D examples. We learn the data-driven models based on simulated rigid body trajectories as training data. Using simulated training data provides a clean ground truth to evaluate the accuracy of the learned models and a first step toward a computationally tractable contact model capable of predicting the behaviors of real-world, near-rigid materials.

II. RELATED WORK

Contact and friction is a common but extremely complex phenomenon, which continuously fascinates generations of scientists and engineers. Coulomb and Amontons in the 18th century made the distinction between static and dynamic frictions [3] and stated the force of friction is directly proportional to the applied load, but independent of apparent contact area and sliding velocity. Hertz in his 1895 work [4] started to treat frictionless contact mechanics more rigorously by considering the local deformation between two elastic bodies. The normal load is then precisely the integrated contact pressure over the patch area where the two bodies meet. Into the 20th century, Carter, Fromm [5] and Kalker [6] incorporated Coulomb's friction law with Hertzian contact to tackle rolling friction problems. Finite element methods for contact problems grew out of these works with the development of modern computers.

On the other line of research, the inadequacies and controversies of Coulomb's law have been extensively studied. For example, Oden and Martins [7] summarized that friction could depend on normal force or stress, normal separation distance, slip displacement, slip velocity, time of stationary contact, slip history, and vibrations. As such, many empirical models that substitute Coulomb's law have been proposed and are summarized in [8]. There is no model that is more accurate than the others in all scenarios. Goyal *et al.* [9] proposed the use of limit surface to enclose all possible friction forces on an object during sliding. Similar to their work, our model works on the rigid-body level instead of point contact level, and loosens the assumptions that friction must oppose direction of motion, and that friction is isotropic.

In computer graphics, animation, and robotics simulation, the simplest Coulomb's law and the point contact representation are often used to approximate contact physics for visualizing or evaluating robotic algorithms. Existing rigid-body simulators often solve a Linear Complementarity Problem (LCP) by enforcing contacts as unilateral constraints and utilizing the complementarity between relative velocities and contact forces [10], [11], [12]. In contrast, Todorov [13] relaxed the contact constraints to solve a convex optimization problem at each time step. Constraint solving methods can be formulated based on force or impulse. The former enforces constraints on acceleration level [10] while the latter enforces constraints implicitly on velocity level [14].

Alternatively, data-driven methods have been applied to approximate physics laws, especially when precise physical models are unavailable or computationally intractable. Grzeszczuk *et al.* [15] trained neural networks to learn the system transition dynamics for generating animations. Hsu and Keyser [16] replaced the collision handling stage with statistical approximators to accelerate large-scale rigid-body simulation. More recently, machine learning methods are used to accelerate fluid simulation [17], [18], [19]. The focus of these approaches has been on the performance of simulation, while our work aims to utilize the expressiveness of statistical models to increase physical fidelity of contact behaviors. Recently, researchers start to investigate the possibility of teaching neural networks the physical intuitions that human possess from vision perception in an end-to-end fashion [20], [21], [22]. In contrast, our work enhances the expressiveness of well studied contact models by learning contact behaviors from observed data, while preserving fundamental contact constraints through analytical expressions.

With the emergence of deep reinforcement learning, the topic of transfer learning from simulation to real world has been actively investigated in the past few years. Most related to our work, Zhou *et al.* [23] built a data-efficient model for the limit surface of an object during planar sliding. Bauza and Rodriguez [24] built a probabilistic model for planer sliding that takes into account the stochasticity of frictional forces. Fazeli *et al.* [25] proposed either to train a purely data-driven model, or to use data to learn the optimal parameters of an analytical model for planer impact. Besides building a more realistic simulation, domain randomization is also a promising approach to sim-to-real transfer [26], [27], [28].

III. METHOD

We propose a method to predict the contact impulse between a specific pair of near-rigid objects. The method enhances the expressiveness of the standard Coulomb contact model by learning the contact behaviors from observed data, while preserving fundamental contact constraints whenever possible. An ideal contact model in a physics simulator should at least guarantee the following properties:

- 1) Non-penetration: The geometry of the objects in contact should not overlap.
- 2) Repulsive force: The contact force should only push the objects away from each other, not pulling them

together.

- 3) Workless condition: The contact force becomes zero at the instance when the bodies begin to separate.
- 4) Two friction regimes: There is a unsmooth switch between static friction forces and dynamic friction forces, which depends on the materials of the objects and other factors.
- 5) Dynamic friction model: The dynamic friction force depends on the normal contact force, the velocity of the object, and other factors.

Among these five properties, (4) and (5) depend on empirical models because their mechanics are not well understood. As such, our method will use a data-driven approach to achieve (4) and (5), while maintaining the analytical solution that satisfies (1)-(3).

A. Assumptions

Our method makes a few assumptions. We address a perfectly inelastic, non-adhesive contact phenomenon between two near-rigid objects with convex shapes. We assume that one of the object is stationary. The deformation during the collision is negligible comparing to the overall rigid body motion. We assume that the time is discretized and the applied forces (i.e. all forces applied on the object except for the constraint force) are integrated prior to solving the constraint force. This assumption simplifies the process for creating samples for training data, but can cause discrepancy between reality and simulated results in some special cases (see more discussion in Section V). Similar to other data-driven approaches, we expect the range of collision impulse encountered at test time to be similar to that during training. For collision between articulated rigid body systems, we assume that the distal rigid body is the only part of the system that is in contact.

We compute the aggregated effect of contact for the entire rigid body, instead of using point-contact representation, which increases computational complexity and leads to issues with over-parameterization. To this end, our method represents the contact geometry as a patch with non-zero area on the surface of the object in contact, denoted as \mathcal{P} . We assume that the normal direction of the contact patch is well-defined.

B. Single rigid body

The contact computation in physics engines typically consists of two separate processes, contact detection and contact handling. The contact detector identifies the contact location on the surface of the object and the contact handler calculates the contact force that satisfies the contact constraints along with the equations of motion. Our work assumes a given contact detector $D(\mathbf{q}_t)$, which takes as input the current position of the rigid body $\mathbf{q}_t \in \mathbb{R}^6$ expressed in the generalized coordinates and outputs the contact patch \mathcal{P} . If $\mathcal{P} = \emptyset$, there is no collision detected between the objects.

The main challenge of contact computation lies in contact handling. In its most general form, a contact handling routine can be expressed as a function $\mathbf{p} = H(\mathbf{q}_t, \dot{\mathbf{q}}_t, \boldsymbol{\tau}, \mathcal{P})$, which

Algorithm 1 Single body contact model

Input: $\mathbf{q}_t, \dot{\mathbf{q}}_t, \boldsymbol{\tau}, \mathcal{P}$

Output: \mathbf{p}

```

1:  $\dot{\mathbf{q}}^{(1)} = \dot{\mathbf{q}}_t + h\mathbf{M}^{-1}\boldsymbol{\tau}$ 
2:  $c \leftarrow C(\mathbf{q}_t, \dot{\mathbf{q}}^{(1)})$ 
3: if  $c == \text{"static"}$  then
4:   AddPositionConstraint( $\mathcal{P}$ )
5:    $\mathbf{p} \leftarrow \text{SolveConstraint}(\mathbf{q}_t, \dot{\mathbf{q}}^{(1)})$ 
6:   RemovePositionConstraint( $\mathcal{P}$ )
7: else if  $c == \text{"dynamic"}$  then
8:    $\mathbf{p}_f \leftarrow R(\mathbf{q}_t, \dot{\mathbf{q}}^{(1)})$ 
9:    $\dot{\mathbf{q}}^{(2)} = \dot{\mathbf{q}}^{(1)} + \mathbf{M}^{-1}\mathbf{T}_f \mathbf{p}_f$ 
10:   $\mathbf{p}_n \leftarrow \text{FrictionlessLCP}(\mathbf{q}_t, \dot{\mathbf{q}}^{(2)})$ 
11:   $\mathbf{p} = \mathbf{T}_n \mathbf{p}_n + \mathbf{T}_f \mathbf{p}_f$ 
12: else
13:    $\mathbf{p} = \mathbf{0}$ 
14: return  $\mathbf{p}$ 

```

maps the pre-contact state (i.e. \mathbf{q}_t and $\dot{\mathbf{q}}_t$), applied forces $\boldsymbol{\tau}$, and contact patch \mathcal{P} to the 6D contact impulse, \mathbf{p} . Precisely, \mathbf{p} is the integrated pressure on the contacting surface over the entire contact patch \mathcal{P} and over the time step interval h . During the collision process, the contact pressure might not be constant, but its aggregated effect in a time step is equivalent to the impulse \mathbf{p} , which can be used to integrate the state forward to the next time step by

$$\dot{\mathbf{q}}_{t+1} = \dot{\mathbf{q}}_t + \mathbf{M}(\mathbf{q}_t)^{-1}(h\boldsymbol{\tau} + \mathbf{p}), \quad (1)$$

$$\mathbf{q}_{t+1} = \text{Integrate}(\dot{\mathbf{q}}_{t+1}), \quad (2)$$

where $\mathbf{M}(\mathbf{q}_t)$ is the generalized mass matrix of the rigid body. At every time step, if D detects a non-empty contact patch \mathcal{P} , we invoke the contact handler H , described in Algorithm 1. We first update the current velocity $\dot{\mathbf{q}}_t$ to an intermediate velocity by explicitly integrating the applied force $\boldsymbol{\tau}$: $\dot{\mathbf{q}}^{(1)} = \dot{\mathbf{q}}_t + h\mathbf{M}^{-1}\boldsymbol{\tau}$.

If we directly train a regressor to predict the contact impulse \mathbf{p} , Properties (1)-(3) are likely to be violated, as they require precise satisfaction of constraints. Instead, we use observed data to train a classifier $C(\mathbf{q}_t, \dot{\mathbf{q}}^{(1)})$ that predicts one of the following outcomes for the contact patch: "static", "dynamic", or "detach". Based on the predicted outcome, we will calculate the contact impulse differently in order to satisfy (1)-(3).

a) Static case: If the classifier outputs "static", we predict that the contact patch will remain in the same position and orientation at the next time step. The contact patch will have zero velocity, but the rigid body is not necessarily stationary. Fig. 1 illustrates an example of the "static" case in which the rigid body is moving while the contact patch is static. The contact impulse in this case must ensure that the contact patch has zero velocity at the end of the time step. In physics engines, this is easily achieved by setting positional constraints at the contact patch and solve for the constraint impulse \mathbf{p} that satisfies $\mathbf{v}_p = \mathbf{0}$, where \mathbf{v}_p is the generalized velocity of \mathcal{P} at the next time step. Since \mathbf{v}_p and \mathbf{p} have the

same effective degrees of freedom (DOFs), the linear system of equations $\mathbf{v}_p(\mathbf{p}) = \mathbf{0}$ has a unique solution. Therefore, if a state is classified as "static" by a highly accurate classifier C , the impulse solution of $\mathbf{v}_p(\mathbf{p}) = \mathbf{0}$ will automatically satisfy Properties (1)-(3).

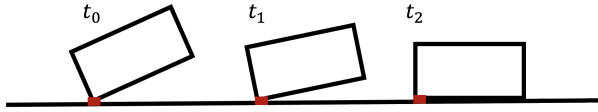


Fig. 1. Illustration of the "static" case. In t_0 and t_1 , the classifier outputs "static". We analytically solve a contact impulse to ensure the contact patch (shown in red) has zero velocity at the end of t_0 and t_1 .

b) Dynamic case: If the classifier outputs "dynamic", we predict that the contact patch will change its position or orientation, or lose some area at the next time step (Fig. 2). In this case, we need to compute the motion of the contact patch by predicting the contact impulse \mathbf{p} . We propose to train a regressor from the observed data because the idealized Coulomb friction model is limited when approximating the complex dynamic friction phenomena. However, directly using a regressor to predict \mathbf{p} will still suffer from the same problem of failing to satisfy Properties (1)-(3) precisely. In a perfectly inelastic case with well-defined contact normal, this issue can be solved by decoupling and re-parameterizing \mathbf{p} into two components: the normal impulse \mathbf{p}_n and the frictional impulse \mathbf{p}_f , parameterized in the wrench space. We still train a regressor $R(\mathbf{q}_t, \dot{\mathbf{q}}^{(1)})$ to predict all six DOFs of the contact impulse, $(\mathbf{p}_f, \mathbf{p}_n)$, as these DOFs are coupled by physics. However, we do not use the predicted normal impulse \mathbf{p}_n . Instead, we transform the predicted frictional impulse \mathbf{p}_f from the friction wrench space to the generalized coordinates of the rigid body using the transformation matrix \mathbf{T}_f and add it to the intermediate velocity, $\dot{\mathbf{q}}^{(2)} = \dot{\mathbf{q}}^{(1)} + \mathbf{M}^{-1}\mathbf{T}_f\mathbf{p}_f$, to obtain a second intermediate velocity $\dot{\mathbf{q}}^{(2)}$. Next, we solve a LCP with frictionless contacts (i.e. solving only for the normal contact impulse) to obtain \mathbf{p}_n , which has a unique solution [29]. Because \mathbf{p}_n satisfies LCP conditions, Properties (1)-(3) are preserved. Finally, we transform both \mathbf{p}_n and \mathbf{p}_f back to the generalized coordinates to obtain the contact impulse \mathbf{p} .

If the regressor R were perfectly accurate, the uniqueness of \mathbf{p}_n ensures that the decoupling treatment in Algorithm 1 will not affect the true solution of contact impulse \mathbf{p} . When R is not perfectly accurate, the decoupling treatment serves as a corrective step on \mathbf{p} to prioritize the satisfaction of Properties (1)-(3) over Property (5).

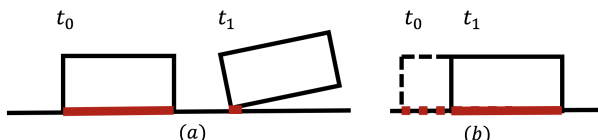


Fig. 2. Illustrations of the "dynamic" case. In both (a) and (b), the classifier outputs "dynamic", because the contact patch (shown in red) at t_0 is moving. The dashed red line indicates that the object is sliding.

c) Detach case: In the "detach" case, the rigid body is predicted to leave the surface at the next time step. Therefore, we set $\mathbf{p} = \mathbf{0}$, ensuring that Property (3) is satisfied.

Remarks: Our method addresses Property (4) by learning a classifier from the observed data. Similarly, the regressor incorporates the observed data to address Property (5). Assuming that the classifier is highly accurate, the resultant contact impulse for the static and detach cases will closely match reality and satisfy Properties (1)-(3) exactly. The classifier will be less accurate near the decision boundary, which coincides with the poorly-understood region where transitions between different physical regimes occur.

C. Articulated rigid bodies

Our method can be extended to handle contact between articulated rigid body systems. We decompose the state of the system into the distal body $(\mathbf{q}_t, \dot{\mathbf{q}}_t)$ and all other bodies in the upstream system $(\hat{\mathbf{q}}_t, \dot{\hat{\mathbf{q}}}_t)$ (Fig. 3). We assume that the distal body is the only part in contact with the other object. If the joint force \mathbf{f}_j transmitted between the distal body and the upstream system is known, we can simply add \mathbf{f}_j to the applied force τ and use Algorithm 1 to compute the contact impulse \mathbf{p} . In reality, \mathbf{f}_j and \mathbf{p} are dependent of each other and need to be solved simultaneously.

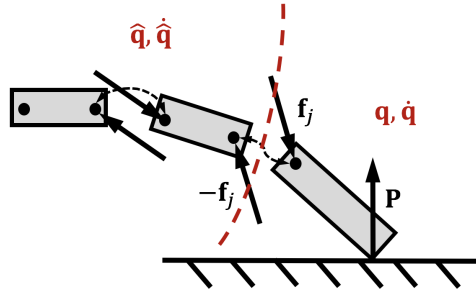


Fig. 3. An articulated rigid body system which consists of a distal body whose state is $(\mathbf{q}, \dot{\mathbf{q}})$ and other bodies in the upstream system $(\hat{\mathbf{q}}, \dot{\hat{\mathbf{q}}})$. We solve for joint constraint force \mathbf{f}_j and contact impulse \mathbf{p} simultaneously.

Our algorithm to solve for the next state of the articulated body system is shown in Algorithm 2, which involves solving a nonlinear system $G(\mathbf{f}_j) = \mathbf{0}$. We start with expressing the velocity of the distal body at the next time step:

$$\dot{\mathbf{q}}_{t+1} = \dot{\mathbf{q}}_t + h\mathbf{M}^{-1}\tau + h\mathbf{M}^{-1}\mathbf{J}^T\mathbf{f}_j + \mathbf{M}^{-1}\mathbf{p}, \quad (3)$$

where $\mathbf{M}(\mathbf{q}_t)$ is the generalized mass matrix for the distal body and $\mathbf{J}(\mathbf{q}_t)$ is the Jacobian transforming from the generalized coordinates of the rigid body to the Cartesian space at the joint. The Cartesian velocity at the joint at the next time step is then given by

$$\mathbf{v}_{t+1} = \mathbf{J}\dot{\mathbf{q}}_t + h\mathbf{J}\mathbf{M}^{-1}\tau + h\mathbf{J}\mathbf{M}^{-1}\mathbf{J}^T\mathbf{f}_j + \mathbf{J}\mathbf{M}^{-1}\mathbf{p}. \quad (4)$$

Similarly, the velocity of the upstream system evaluated at the joint can be expressed as

$$\hat{\mathbf{v}}_{t+1} = \hat{\mathbf{J}}\dot{\hat{\mathbf{q}}}_t + h\hat{\mathbf{J}}\hat{\mathbf{M}}^{-1}\hat{\tau} - h\hat{\mathbf{J}}\hat{\mathbf{M}}^{-1}\hat{\mathbf{J}}^T\mathbf{f}_j, \quad (5)$$

where $\hat{\mathbf{M}}$ and $\hat{\mathbf{J}}$ are the mass matrix and Jacobian for the upstream system.

Algorithm 2 Articulated bodies contact solver

Input: $(\mathbf{q}_t, \dot{\mathbf{q}}_t, \boldsymbol{\tau}), (\dot{\mathbf{q}}_t, \ddot{\mathbf{q}}_t, \ddot{\boldsymbol{\tau}}), \mathcal{P}$
Output: $\mathbf{q}_{t+1}, \dot{\mathbf{q}}_{t+1}, \ddot{\mathbf{q}}_{t+1}, \ddot{\boldsymbol{\tau}}_{t+1}$

- 1: Initialize \mathbf{f}_j using Eq. 7
- 2: Calculate $\mathbf{J}, \mathbf{M}, \hat{\mathbf{J}}, \hat{\mathbf{M}}$
- 3: **while** solver not terminated **do**
- 4: Evaluate $G(\mathbf{f}_j)$ using Eq. 6
- 5: Update \mathbf{f}_j according to Powell's method
- 6: $\mathbf{p} \leftarrow H(\mathbf{q}_t, \dot{\mathbf{q}}_t, \boldsymbol{\tau} + \mathbf{J}^T \mathbf{f}_j, \mathcal{P})$
- 7: $\dot{\mathbf{q}}_{t+1} = \dot{\mathbf{q}}_t + h\mathbf{M}^{-1}\boldsymbol{\tau} + h\mathbf{M}^{-1}\mathbf{J}^T \mathbf{f}_j + \mathbf{M}^{-1}\mathbf{p}$
- 8: $\mathbf{q}_{t+1} = \text{Integrate}(\mathbf{q}_t, \dot{\mathbf{q}}_{t+1})$
- 9: $\ddot{\mathbf{q}}_{t+1} = \ddot{\mathbf{q}}_t + h\hat{\mathbf{M}}^{-1}\ddot{\boldsymbol{\tau}} - h\hat{\mathbf{M}}^{-1}\hat{\mathbf{J}}^T \mathbf{f}_j$
- 10: $\ddot{\boldsymbol{\tau}}_{t+1} = \text{Integrate}(\ddot{\mathbf{q}}_t, \ddot{\mathbf{q}}_{t+1})$
- 11: **return** $\mathbf{q}_{t+1}, \dot{\mathbf{q}}_{t+1}, \ddot{\mathbf{q}}_{t+1}, \ddot{\boldsymbol{\tau}}_{t+1}$

Since the joint constraint is satisfied at the beginning of the time step t_0 , we only need to ensure that the velocity of the constraint is satisfied so that at t_1 the distal body and the upstream system coincide at the joint. Therefore, we need to solve for a \mathbf{f}_j such that $\mathbf{v}_{t+1} - \hat{\mathbf{v}}_{t+1} = \mathbf{0}$:

$$G(\mathbf{f}_j) = \mathbf{v}_{t+1} - \hat{\mathbf{v}}_{t+1} = \mathbf{A}\mathbf{f}_j + \mathbf{J}\mathbf{M}^{-1}H(\mathbf{f}_j) + \mathbf{c} = \mathbf{0}, \quad (6)$$

where $\mathbf{A} = h\mathbf{J}\mathbf{M}^{-1}\mathbf{J}^T + h\hat{\mathbf{J}}\hat{\mathbf{M}}^{-1}\hat{\mathbf{J}}^T$ and $\mathbf{c} = \mathbf{J}\dot{\mathbf{q}}_t + h\mathbf{J}\mathbf{M}^{-1}\boldsymbol{\tau} - (\hat{\mathbf{J}}\dot{\mathbf{q}}_t + h\hat{\mathbf{J}}\hat{\mathbf{M}}^{-1}\ddot{\boldsymbol{\tau}})$ are constants in the equation given the current state vectors. $H(\mathbf{f}_j)$ is a shorthand for $H(\mathbf{q}_t, \dot{\mathbf{q}}_t, \boldsymbol{\tau} + \mathbf{J}^T \mathbf{f}_j, \mathcal{P})$, which outputs the contact impulse \mathbf{p} depending on \mathbf{f}_j .

We solve Eq. 6 using Powell hybrid method [30], which uses finite difference to approximate the Jacobian matrix and is less sensitive to the initial guess to the problem. Powell's method only requires a routine to evaluate $G(\mathbf{f}_j)$ and an initial guess. Using the heuristic that assumes $\hat{\mathbf{v}}_{t+1} = \mathbf{0}$, we compute the initial \mathbf{f}_j by

$$\mathbf{f}_j = (h\hat{\mathbf{J}}\hat{\mathbf{M}}^{-1}\hat{\mathbf{J}}^T)^{-1}\hat{\mathbf{J}}(\dot{\mathbf{q}}_t + h\hat{\mathbf{M}}^{-1}\ddot{\boldsymbol{\tau}}). \quad (7)$$

In our experiments a solution can always be found at each time step with 0.5% convergence tolerance. The number of evaluations of G is often fewer than 10.

D. Implementation

A contact patch in the real world will always be a 2D surface. However, when the contact patch degenerates to nearly an edge or a point, in practice, the dimension of controllable space of the friction impulse will reduce. Since the dimension of contact patch is available from the collision detector D , we utilize this information to improve learning accuracy by treating three types of contact patches separately: a surface (2D), a line (1D), or a point (0D). For each type, we train a specific classifier (C_2, C_1 , or C_0) and a regressor (R_2, R_1 , or R_0). Using separate neural networks allows the regressors to have different output dimensions according to the dimension of controllable space of the friction impulse.

The same set of training data can be used to train the classifiers and the regressors. Since the applied force is integrated and added to the current velocity prior to solving

the constraint force, we can collect the training data by simply throwing the objects to each other with different initial velocities. We record the entire trajectory for each throw and extract the state of every contact instance: $\mathbf{q}_t, \dot{\mathbf{q}}_t$. By comparing \mathbf{q}_t to its next state \mathbf{q}_{t+1} , we can identify and label static and dynamic cases. To determine detach cases and compute the output values for the regressors, we need to recover the contact impulse \mathbf{p} for each contact instance: $\mathbf{p} = \mathbf{M}(\dot{\mathbf{q}}_{t+1} - \dot{\mathbf{q}}_t) - h\boldsymbol{\tau}$. If \mathbf{p} is almost zero, we label this contact instance "detach".

The range of initial throwing velocities determines the distribution of our training samples. The range should be chosen such that it well covers the anticipated collision impulses in the test set. To mitigate the number of throws needed for creating an unbiased training dataset, in the simulated environment, one can directly uniformly sample the subset of state space in which the objects are in contact, set the state of the object to the sampled values, and forward simulate for one time step. When collecting data from the real world, a robotic instrument can be used to precisely control the state of the object to create desired contact instances.

IV. EVALUATION

We evaluate our data-augmented contact model on 2D rigid bodies with different shapes and a 3-linked articulated rigid body chain. We also test the algorithm on objects with anisotropic friction coefficient. The data are collected in a simulated environment and the model is also tested in simulation. Though the 2D implementation is simpler and has fewer Dofs than 3D, the predicted error in 2D can still accumulate quickly and lead to large discrepancy over time. We use a generic physics engine DART [31] to implement all our experiments.

The training set for each experiment contains 50,000 samples. Each classifier or regressor consists of three hidden layers with 32-32-16 neurons. A standard cross-entropy error/MSE is used for the loss function. The training of each neural network takes only a few minutes on a Core i5 CPU without any GPU support. For the two rigid bodies we evaluated, a rectangle and a pentagon, C_0 and R_0 reach 95% accuracy; C_1 and R_1 have a slightly higher accuracy of 98%.

We evaluate our results against two baselines. The first baseline serves as the ground truth (GS), which computes contact impulses by using the same contact handling routine (i.e. LCP solver in DART) used to collect the training data. The second baseline is a pure data-driven (PDD) approach which learns a regressor to predict the contact impulse from the state of the object, without first identifying the contact state using a classifier. The size of training data, the network architecture, and the learning algorithm are the same between PDD and our method. The trained regressors for PDD also reach 95% accuracy for both \tilde{R}_0 and \tilde{R}_1 .

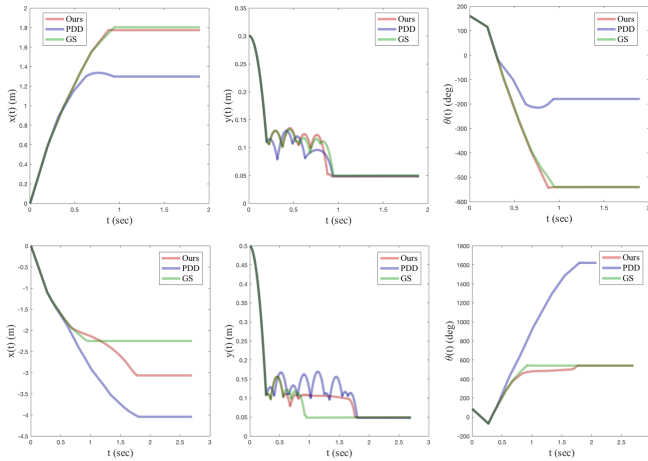


Fig. 4. Motion trajectories of Trial 7 (Top) and Trial 5 (Bottom).

A. Rectangle

In this experiment, a rectangle is thrown from the initial position (x_0, y_0, θ_0) and velocity $(\dot{x}_0, \dot{y}_0, \dot{\theta}_0)$ to the ground under gravity. We conduct 10 trials with various height from the ground y_0 and various velocity \dot{x}_0 and $\dot{\theta}_0$. Note that x_0 is fixed to zero because we only concern about the horizontal distance the object travels, not the horizontal initial position. We also fix \dot{y}_0 to zero because we can change the vertical velocity at the first instance of impact by adjusting the initial height y_0 . The other four initial conditions are randomly chosen approximately within the training data range.

Fig. 5 shows the results of the 10 trials in comparison with two baselines, GS and PDD. We measure the number of bounces, the horizontal distance traveled, and the final orientation of the rectangle. In most cases, our method matches GS closely and significantly better than PDD, demonstrating the advantages of using classifier and analytical solutions. We select one of the best trials (Trial 7) and one of the worst trials (Trial 5) and show the trajectories of position and orientation in Fig. 4 top and bottom respectively. In Trial 7, our trajectories match the GS's trajectories very closely, but PDD predicts fewer bounces and dissipates energy too quickly, resulting in less distance traveled and a different final orientation. In Trial 5, although the number of bounces and the final orientation of our method match the GS, the characteristics of the motion is quite different. After the object bounces a few times, our method does not generate enough friction to stop the object, resulting in longer distance traveled. PDD also performs poorly in this trial. It exhibits more energetic motion, leading to many more bounces, much larger final orientation angle, and even longer distance traveled than ours. It is worth noting that PDD sometimes results in interpenetration with the ground as evidenced by the fact that the final orientation angle is not always a multiple of 90° . For example, the penetration in Trial 4 is particularly visible.

There are around 200 contact instances classified as static in the 10 trials we evaluate. None of these instances violates the repulsive force condition (2), showing that using posi-

trial	y_0	θ_0	\dot{x}_0	$\dot{\theta}_0$	number of bounces			distance traveled			final orientation		
					Ours	GS	PDD	Ours	GS	PDD	Ours	GS	PDD
1	0.25	131.8	3.5	4	0	0	0	0.763	0.838	0.857	179	180	187
2	0.33	0.0	4.2	45	0	0	5	1.484	1.671	2.427	359	360	-177
3	0.7	-114.6	2	0	0	0	2	0.881	0.877	1.006	-180	-180	-270
4	0.35	57.3	-1	-30	1	2	1	-0.27	-0.277	-0.061	-271	-270	-340
5	0.5	85.9	-4	-10	5	5	11	-3.06	-2.250	-4.041	540	540	1624
6	1	-40.1	-0.5	0.5	1	0	0	-0.3	-0.289	-0.384	1	2	0
7	0.3	160.4	3	-4	8	8	5	1.773	1.803	1.298	-541	-540	-179
8	0.25	-171.9	-2.5	0	0	0	0	-0.51	-0.534	-0.511	-180	-180	-181
9	0.4	115	3	0	7	7	4	1.707	1.685	1.366	-450	-360	-180
10	0.4	28.6	3	20	5	5	6	1.309	1.310	1.722	-92	0	-180

Fig. 5. The rectangle experiment.

trial	y_0	θ_0	\dot{x}_0	$\dot{\theta}_0$	number of bounces			distance traveled			final orientation		
					Ours	GS	PDD	Ours	GS	PDD	Ours	GS	PDD
1	0.5	-114.650	3	0	1	1	1	0.954	0.888	-159	-159	-158	-158
2	0.6	-85.987	2	3	1	1	1	0.402	0.515	-33	0	0	0
3	0.6	171.975	4	-5	4	4	4	1.958	2.059	-227	-227	-225	-225
4	0.38	103.185	-2.5	20	4	4	4	-1.083	-1.139	565	562	562	562
5	0.3	11.465	-3.6	2	2	2	2	-1.129	-1.064	202	202	202	202
6	0.9	-166.242	-1	30	5	5	5	-1.604	-1.558	926	926	922	922
7	0.7	177.707	0.5	-40	4	4	4	0.857	0.928	-884	-884	-879	-879
8	0.26	0.000	3.9	0	1	1	1	1.188	1.488	-159	-158	-158	-158
9	0.45	-63.057	2.7	-10	4	5	5	1.255	1.291	-405	-405	-405	-405
10	0.25	-154.777	-4.5	0	0	0	0	-0.840	-1.336	-158	-158	-158	-158

Fig. 6. The pentagon experiment.

tional constraints in the static case could suffice in practice given a highly accurate classifier.

B. Pentagon

We conduct the same experiment on a irregular pentagon thrown to the ground 10 times. The difference in shape does not affect our algorithm, but it significantly slows down the GS baseline. This is because, unlike a rectangle which is a primitive shape supported by the collision detector, the geometry of a pentagon is represented as a triangular mesh which typically results in more contact points than a primitive shape. Consequently, the contact handler used by GS ends up solving much larger LCP problems. In contrast, our method does not depend on the number of the contact points and thus has no difference in performance between simulating primitives and meshes.

Fig. 6 shows the comparison between our method and GS for the pentagon experiment. Similar to the rectangle, our method matches GS closely, with the exception of Trial 10, in which a large distance error is accumulated due to a long period of sliding motion (see Section V for more discussion).

C. Capsule

To demonstrate that our method can also be applied to objects with curvy geometries, a capsule trained with our model is dropped to the ground. Fig. 7 compares the motion sequence produced by our method and by the LCP solver in DART. The two motions appear visually identical. In this example, it is interesting to note that all contact instances are classified as "static", due to the fact that the tip of capsule undergoes perfect rolling before resting on the ground. The positional constraint added ensures that the relative velocity at the contact point at the end of each time step is zero, consistent with the definition of perfect rolling. Since the constraint is removed and a new constraint is added at a



Fig. 7. Motion of a falling capsule using our method (Left) and GS (Right). Though the visualization appears in 3D, the motion is in 2D with zero values in z-axis.

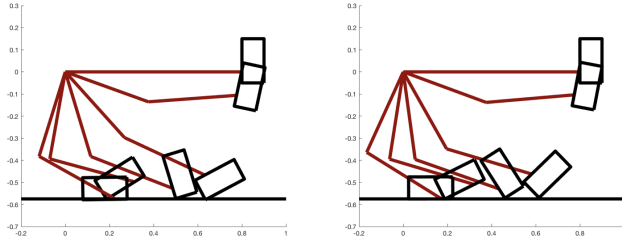


Fig. 8. Simulated trajectories of a swinging chain by our (Left) and GS (Right) methods.

different location at next time step, the capsule is never “locked” during rolling.

D. 3-linked chain

We demonstrate our method on an articulated rigid body system with three links connected by two revolute joints. The top of the first link is pinned to a fixed location in the world space. The chain starts at a horizontal position and swings passively to the ground under gravity. We compare our method to DART’s LCP solver and show the motion sequences in Fig. 8. Though our method is only trained on the contact instances between an isolated distal body (i.e. the third link) and the ground, we show that both contact impulse and the joint constraint force can be predicted accurately. We compare the violations at the distal joint between our method and DART’s LCP solver and visualize the difference using a histogram (Fig. 9).

E. Anisotropic friction cone

We create a fictitious material which has an anisotropic friction cone. The friction coefficient is 1.5 if the horizontal velocity at the contact is negative, and 0.75 if positive. We collect the training data from this simulated scenario and learn the classifiers and regressors using the same algorithms. Fig. 10 shows the motion sequences of throwing a rectangle to the ground using our contact model (top) and using the GS simulator (bottom). Similar to GS, our model predicts different final resting positions when the object is thrown in two opposite directions.

V. CONCLUSION AND LIMITATIONS

We introduce a *data-augmented* contact model that predicts the contact behaviors for a particular pair of near-rigid bodies or articulated rigid body systems. Our method utilizes

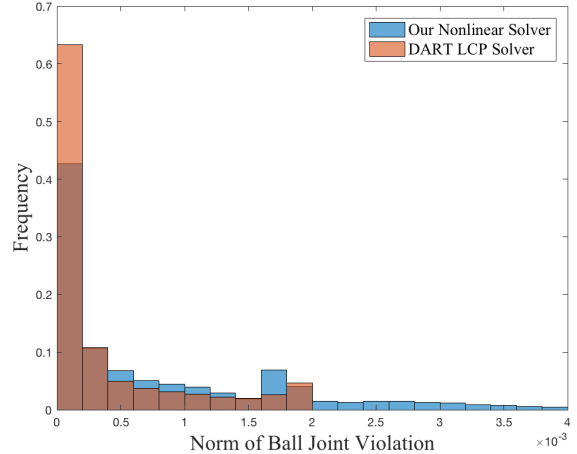


Fig. 9. Distributions of the norm of the distal joint violations in simulated trajectories by our (blue) and GS (orange) methods.

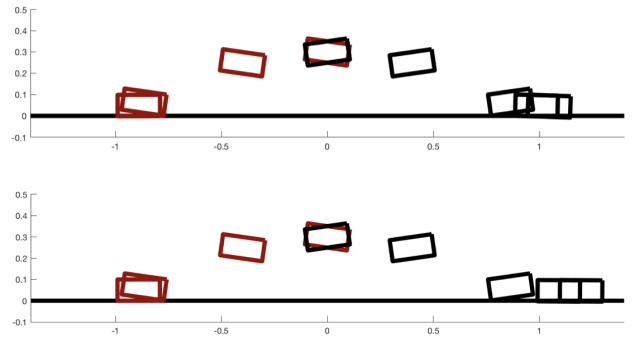


Fig. 10. Simulated trajectories of a box thrown in opposite directions (red/black) by our (Top) and GS (Bottom) methods. The friction coefficient is anisotropic.

analytical solutions based on fundamental contact constraints whenever possible, while leveraging observed data when the phenomenon is less well understood. We evaluate our method on a set of 2D examples using simulated training data. The promising results indicate that our work could be a first step toward a computationally tractable contact model capable of predicting the behaviors of the real-world, near-rigid materials.

Though our regressors can reach 95% accuracy, the artifact becomes visible when the object is sliding on the surface for an extended period of time. This phenomenon is due to the fact that the neural network has larger relative errors, $\frac{\|\hat{y} - y\|}{\|y\|}$, when the ground truth value is small. Here \hat{y} is the predicted value and y is the ground truth. Comparing to the time instances of impact, the magnitude of friction impulse is significantly smaller when the object is simply sliding on the surface, hence the larger relative error. Compounding with accumulated prediction errors over time, the sliding case ends up being the most challenging scenario for our method. In an attempt to mitigate the issue, we have tried to use Mean Absolute Percentage Error (MAPE) as the

loss function during training, instead of the standard MSE. However, MAPE tends to make stochastic gradient descent unstable as the losses for small samples become unbounded above. One possible solution is to train a separate regressor specifically for very small frictional impulses.

Our method assumes that the applied forces can be integrated prior to solving the constraint force. This assumption is not true for some special cases. Consider, in Case A, a 1kg object with zero initial velocity on a surface is under an applied force \mathbf{f} horizontal to the surface, and in Case B, without an external force, the same object has a initial velocity $h\mathbf{f}$. If the magnitude of \mathbf{f} happens to be $\mu_d g < \|\mathbf{f}\| < \mu_s g$, where μ_d and μ_s are the kinetic and static friction coefficients and g is the magnitude of gravitational force applied on the object, Case A will have zero velocity while Case B will have a velocity of $h\|\mathbf{f}\| - h\mu_d g$ at the end of the time step. One possible way to address this issue is to include τ as part of the input vector to the neural networks, instead of integrating it into $\dot{\mathbf{q}}_t$. We can also represent the applied force as a distribution of forces instead of a single aggregated force vector. This representation might produce more accurate prediction for small-scale contact impulses.

When collecting the training data from the real world, an isolated distal part of the robot will be used to create the collisions with the surface. The range of collision impulses should cover that of the anticipated collisions during the operation of the full robot. Although the data collection can be conducted in isolation without involving the entire robot, the data-efficiency remains a major concern. Since the dimension of the input and output space is relatively low, it is possible to use other function approximators, such as support vector machines or Gaussian processes, which might be more data-efficient than neural networks.

Finally, our current algorithm assumes that one of the objects is stationary, and does not handle simultaneous contacts of multiple bodies, which limits its usage in many manipulation tasks. As immediate future directions, we plan to extend Algorithm 1 to two moving bodies by including states of both objects as input.

REFERENCES

- [1] C. Lemke and J. Howson, “Equilibrium points of bimatrix games,” *SIAM Journal on Applied Mathematics*, vol. 12, 1964.
- [2] F. Jourdan, P. Alart, and M. Jean, “A gauss-seidel like algorithm to solve frictional contact problems,” *Computer Methods in Applied Mechanics and Engineering*, vol. 155, 1998.
- [3] E. Popova and V. L. Popov, “The research works of Coulomb and Amontons and generalized laws of friction,” *Friction*, vol. 3, 2015.
- [4] H. Hertz, “On contact between elastic bodies,” *Gesammelte Werke (Collected Works)*, 1895.
- [5] K. Knothe, “History of wheel/rail contact mechanics: from redtenbacher to kalker,” *Vehicle System Dynamics*, vol. 46, pp. 9–26, 2008.
- [6] J. J. Kalker, *On the rolling contact of two elastic bodies in the presence of dry friction*. PhD thesis, Delft University of Technology, 1967.
- [7] J. Oden and J. Martins, “Models and computational methods for dynamic friction phenomena,” *Computer methods in applied mechanics and engineering*, vol. 52, 1985.
- [8] H. Olsson, K. J. Åström, C. C. De Wit, M. Gäfvert, and P. Lischinsky, “Friction models and friction compensation,” *Eur. J. Control*, vol. 4, no. 3, pp. 176–195, 1998.
- [9] S. Goyal, A. Ruina, and J. Papadopoulos, “Limit surface and moment function descriptions of planar sliding,” in *Robotics and Automation (ICRA), 1989 IEEE International Conference on*, pp. 794–799, IEEE, 1989.
- [10] D. Baraff, “Analytical methods for dynamic simulation of non-penetrating rigid bodies,” in *ACM SIGGRAPH Computer Graphics*, vol. 23, pp. 223–232, ACM, 1989.
- [11] D. Stewart and J. C. Trinkle, “An implicit time-stepping scheme for rigid body dynamics with Coulomb friction,” in *Robotics and Automation (ICRA), 2000 IEEE International Conference on*, vol. 1, pp. 162–169, IEEE, 2000.
- [12] M. Anitescu and F. A. Potra, “A time-stepping method for stiff multibody dynamics with contact and friction,” *International Journal for Numerical Methods in Engineering*, vol. 55, 2002.
- [13] E. Todorov, “Convex and analytically-invertible dynamics with contacts and constraints: Theory and implementation in MuJoCo,” *Robotics and Automation (ICRA), 2014 IEEE International Conference on*, pp. 6054–6061, 2014.
- [14] B. V. Mirtich, *Impulse-based Dynamic Simulation of Rigid Body Systems*. PhD thesis, University of California at Berkeley, 1996.
- [15] R. Grzeszczuk, D. Terzopoulos, and G. Hinton, “Neuro animator: Fast neural network emulation and control of physics-based models,” in *Proceedings of the 25th annual conference on Computer graphics and interactive techniques*, pp. 9–20, ACM, 1998.
- [16] S.-W. Hsu and J. Keyser, “Statistical simulation of rigid bodies,” in *Proceedings of the 2009 ACM SIGGRAPH/Eurographics Symposium on Computer Animation*, pp. 139–148, ACM, 2009.
- [17] S. Jeong, B. Solenthaler, M. Pollefeys, M. Gross, et al., “Data-driven fluid simulations using regression forests,” *ACM Transactions on Graphics (TOG)*, vol. 34, no. 6, p. 199, 2015.
- [18] C. Yang, X. Yang, and X. Xiao, “Data-driven projection method in fluid simulation,” *Computer Animation and Virtual Worlds*, vol. 27, no. 3-4, pp. 415–424, 2016.
- [19] J. Tompson, K. Schlachter, P. Sprechmann, and K. Perlin, “Accelerating eulerian fluid simulation with convolutional networks,” in *International Conference on Machine Learning*, pp. 3424–3433, 2017.
- [20] M. Chang, T. Ullman, A. Torralba, and J. B. Tenenbaum, “A compositional object-based approach to learning physical dynamics,” in *Proceedings of the 5th International Conference on Learning Representations*, 2016.
- [21] A. Byravan and D. Fox, “Se3-nets: Learning rigid body motion using deep neural networks,” in *Robotics and Automation (ICRA), 2017 IEEE International Conference on*, pp. 173–180, IEEE, 2017.
- [22] A. Lerer, S. Gross, and R. Fergus, “Learning physical intuition of block towers by example,” in *International Conference on Machine Learning*, pp. 430–438, 2016.
- [23] J. Zhou, R. Paolini, J. A. Bagnell, and M. T. Mason, “A convex polynomial force-motion model for planar sliding: Identification and application,” in *Robotics and Automation (ICRA), 2016 IEEE International Conference on*, pp. 372–377, IEEE, 2016.
- [24] M. Bauza and A. Rodriguez, “A probabilistic data-driven model for planar pushing,” in *Robotics and Automation (ICRA), 2017 IEEE International Conference on*, pp. 3008–3015, IEEE, 2017.
- [25] N. Fazeli, S. Zapolsky, E. Drumwright, and A. Rodriguez, “Learning data-efficient rigid-body contact models: Case study of planar impact,” in *Conference on Robot Learning*, pp. 388–397, 2017.
- [26] J. Tobin, R. Fong, A. Ray, J. Schneider, W. Zaremba, and P. Abbeel, “Domain randomization for transferring deep neural networks from simulation to the real world,” in *Intelligent Robots and Systems (IROS), 2017 IEEE/RSJ International Conference on*, pp. 23–30, IEEE, 2017.
- [27] W. Yu, C. K. Liu, and G. Turk, “Preparing for the unknown: Learning a universal policy with online system identification,” *Robotics Science and Systems (RSS)*, 2017.
- [28] X. B. Peng, M. Andrychowicz, W. Zaremba, and P. Abbeel, “Sim-to-real transfer of robotic control with dynamics randomization,” *arXiv preprint arXiv:1710.06537*, 2017.
- [29] D. Baraff, *Dynamic Simulation of Non-penetrating Rigid Bodies*. PhD thesis, Cornell University, 1992.
- [30] M. J. Powell, “A hybrid method for nonlinear equations,” *Numerical methods for nonlinear algebraic equations*, 1970.
- [31] J. Lee, M. X. Grey, S. Ha, T. Kunz, S. Jain, Y. Ye, S. S. Srinivasa, M. Stilman, and C. K. Liu, “DART: Dynamic animation and robotics toolkit,” *The Journal of Open Source Software*, 2018.